# CrystEngComm

Accepted Manuscript






ROYAL SOCIETY OF CHEMISTRY

www.rsc.org/crystengcomm

# Morphology mediated tailoring the performance of porous nanostructured $Mn_2O_3$ as anode material

Provas Pal,[a] Arnab Kanti Giri,[a] Sourindra Mahanty,[b,*] Asit Baran Panda [a,*]

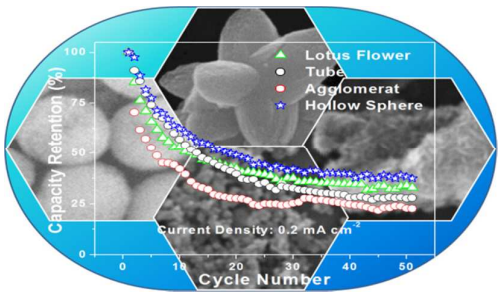


Morphology mediated performance as anode material in Li-ion battery of synthesized porous $Mn_2O_3$ with varying shapes is presented.

Journal Name

RSCPublishing

ARTICLE

# Morphology mediated tailoring the performance of porous nanostructured $Mn_2O_3$ as anode material

Cite this: DOI: 10.1039/xoxxoooooox

Provas Pal,[a] Arnab Kanti Giri,[a] Sourindra Mahanty, [b,]* Asit Baran Panda [a,]*

Received ooth January 2012,
Accepted ooth January 2012

DOI: 10.1039/xoxxoooooox

www.rsc.org/

Tailoring of functional properties through variation of size and shape of porous nanostructured materials is an important area of present frontier research. Herein, we report successful synthesis of nanostructured $Mn_2O_3$ with desired 3D architecture such as, porous hollow sphere, lotus shaped and tubular, as well as aggregated nanoparticles through the calcination of corresponding $MnCO_3$ with identical architecture. Porous hollow structures were formed due to the evolution of $CO_2$ during decomposition of carbonate intermediate and hollow structure was formed through nonequilibrium interdiffusion process, i.e., Kirkendall effect. The bare $MnCO_3$ architecture were synthesized through chelating agent; citric acid (CA), tartaric acid (TA), oxalic acid (OA), and ethylenediaminetetraacetic acid (EDTA); mediated growth by hydrothermal treatment of precursor solution containing $MnCl_2$, ammonium carbonate and chelating agent. A systematic evaluation of morphology mediated performance of these synthesized $Mn_2O_3$ as anode material in Li-ion battery reveal that the shape and the nature of pores of $Mn_2O_3$ strongly influences its Li- ion storage capacity. A superior specific capacity of 478 $mAhg^{-1}$ is obtained for hollow spheres with 38% retention after 30 cycles compared to other shapes due its high accessible surface area and inner hollow architecture.

## Introduction.

Tailoring of physico-chemical properties through the modification of size and morphology of nanostructured materials are the one of the most important fundamental issue in nanoscience and technology.[1] Thus, tremendous research efforts have been made on the synthesis of size and shape selective nanostructure materials, which includes, 0D spheres, 1D rod, wire, tube, 2D sheet, plate and evaluation of their novel properties.[2-3] Although these materials showed size and shape selective improved properties, but for tremendous agglomeration origination from high surface energy, which leads to reduced effective surface area and low tap density, restricts them for some specific surface active applications like, catalysis, solar cells, sensor, Li-ion batteries etc.[4] Where as 3D assembled hierarchical micro- /nano-structures have some unique properties towards high tap density and porous nature increase the molecular transportation through the structure due to high surface area. Hence, design and synthesis of 3D assembled hierarchical micro- /nano-structures constructed of these lower dimensional materials towards a specific stable geometric architecture offers the opportunity to study the structure–property relations as well as diverse material fabrication techniques.[5] Further, the activity of these 3D architectures for the mentioned surface active application are not only related to their morphology and microstructure but also to their porosity and specific arrangement, which offers negligible diffusion rate and favourable kinetics for enhanced properties, such as, hollow nanostructures offer improved properties for their favorable microstructures and sufficient interior space.[6]

Manganese oxide, an important transition metal oxide, has been investigated extensively and considered to be the technologically important material in catalysis, molecular adsorption, magnetism, Li-ion batteries for their diverse structural and compositional flexibility and novel physico-chemical properties.[7-16] In recent years, $Mn_2O_3$, a polymorph of manganese oxides, has gained tremendous interest as an important catalyst for the oxidation of carbon mono-oxide, different pollutant organic molecules and as anode material in Li-ion battery as well.[8-16] As it is abundant, cheap, environmentally benign, and hold high theoretical specific capacity (~1018 $mAhg^{-1}$), $Mn_2O_3$ is considered to be a suitable alternative as anode material for Li-ion battery. However, its use is restricted for poor achievable capacity due to low intrinsic conductivity and capacity fading with cycling. [12-13, 15] In order to improve the electrochemical properties, $Mn_2O_3$ with varying shapes, like rod, wire, octahedral, as well as 3D assembled hierarchical porous structure, have been synthesized.[8-19] It is found that the porous structures helped achieving a higher energy density and hollow structure also improved cycle performance. Qiu *et al.*[18] have hydrothermally synthesized oval-shaped hierarchical structures and achieved a specific capacity of ~380 $mAhg^{-1}$ after 150 cycles for straw-sheaf-shaped $Mn_2O_3$. On the other hand, hollow rod-like $Mn_2O_3$, synthesized from bacterial templates showed a specific capacity of ~ 300 $mAhg^{-1}$.[20] Recently, Li *et al.*[21] have shown that Cu-doped hollow spherical $Mn_2O_3$ exhibited a specific capacity of

642 $mAhg^{-1}$ after 100 cycles at a current density of 100 $mAg^{-1}$. Among the developed strategies for 3D assembled porous architectures, synthesis through calcination of intermediate (e.g., carbonate, glycolate) with specific structure is the most appealing and widely studied, which mainly resulted in spherical hollow structures. This restricts a systematic evaluation of morphology mediated tailoring the performance of $Mn_2O_3$ as anode material, thus far. [8-10, 13-15]

Recently, we have developed a simple aqueous solution based chelating ligands, such as citric acid (CA), tartaric acid (TA), oxalic acid (OA), and ethylenediaminetetraacetic acid (EDTA) mediated growth of hierarchically assembled shapes of $MnCO_3$ with a reasonable degree of control over the resulting structure.[19] This motivated us to verify the probability for the formation of porous $Mn_2O_3$ with controlled hierarchical structures from the synthesized $MnCO_3$ and systematically evaluate their morphology mediated electrochemical performance as anode material for Li-ion battery.

Herein, we report the synthesis of porous $Mn_2O_3$ with different shapes; as porous hollow sphere, lotus shaped and tubular, and aggregated nanoparticles without any specific shape; through the calcination of corresponding $MnCO_3$ and their systematic morphology mediated performance as anode material in Li-ion battery.

## Experimental.

### Chemicals.

Manganous chloride AR [$MnCl_2.4H_2O$], citric acid anhydrous LR [CA, $C_6H_8O_7$, MW-192.13], tartaric acid LR, [TA, $C_4H_6O_6$, MW-150.087], oxalic acid dihydrate LR [OA, $C_2H_2O_4$, MW-126.07], Ethylenediamintetra acetic acid (EDTA, $C_{10}H_{16}N_2O_8$, MW- 292.24] and ammonium carbonate were purchased from S. D. Fine Chemical, India. All the chemicals were used without further purification. For all applications, water with a resistivity of 18 MΩ $cm^{-1}$ was used, obtained from a Millipore water purifier.

### Synthesis of orthorhombic $Mn_2O_3$ with different morphologies.

The different morphologies of orthorhombic $Mn_2O_3$ were synthesized through the manganese carbonate intermediate, [19] which on calcination at 500°C for 6h resulted in the desired product. In a typical synthesis for Hierarchical Lotus shaped Manganese carbonate, aqueous solution of ammonium carbonate (4 g, 0.025 mol) was added to a pre-mixed solution of manganous chloride AR [$MnCl_2.4H_2O$, 2g, 1.01x10-2 mol) and citric acid anhydrous (2g, 1.04x10-2 mol) solution to make the total volume 40 mL. The clear solution was transferred to 60 mL Teflon-lined stainless steel autoclave and sealed properly. The autoclave was placed in a pre-heated oven at 150 °C for 12 h. After that, the autoclave was allowed to cool to room temperature and the resultant precipitates were collected by centrifugation, thoroughly washed with water followed by ethanol and dried at 90 °C/12 h. Finally, the dried powder was calcined at 500 °C for 6 h to get the corresponding $Mn_2O_3$, respectively. For the other shapes like hollow sphere, tube and aggregated particles, the similar synthetic methodology was adopted, as mentioned above, just using the equivalent amount of oxalic acid, tartaric acid and EDTA, respectively, instead of citric acid.

### Characterizations.

Powder X-ray diffraction patterns of the samples were obtained from a Rigaku MINIFLEX-II (FD 41521) powder diffractometer. The thermo-gravimetric analysis (TGA) of the hierarchical shaped $MnO_2$ was obtained from a Mettler- Toledo (TGA/SDTA 851e) instrument. The nitrogen adsorption-desorption measurements were carried out using an ASAP 2010 Micromeritics, USA to know the textural properties of the synthesized $MnO_2$ samples. To determine the morphology of samples the scanning electron microscope (SEM) micrographs were obtained from a Leo series 1430 VP. Transmission electronic microscope (TEM) images of the $Mn_2O_3$ samples were recorded using a JEOL JEM 2100 microscope. X-ray photoelectron spectroscopy (XPS) was performed using a Multilab-2000 (Thermo-scientific UK) spectrometer using a monochromic MgKR X-ray source (1256 eV) with an analyser pass energy of 10 eV Samples were mounted on SS sample holder with silver paint. Details of all the performed characterization procedures and sample preparation techniques were followed as mentioned in our previous report.[44]

### Electrochemical Application.

Electrochemical properties of the prepared $Mn_2O_3$ samples were evaluated by fabricating coin cells vs $Li/Li^+$. For fabrication of a typical electrode, first a slurry was made by mixing $Mn_2O_3$ powder (75 wt%), acetylene black (15 wt%) and PVDF binder (10 wt%) in n-methyl pyrrolidinone (NMP) solvent. Then, the slurry was coated onto a 15 µm thick copper foil (current collector) and dried at 110°C in an oven for 12 h. After pressing the coated foil at 4.0 ton $inch^{-2}$, circular disks of 15 mm in diameter were cut and used as electrode. Typical weight of the active material (excluding acetylene black and PVDF) was ~7 mg. Coin cells (2032 type) were assembled with these electrodes using Li metal as counter as well as reference electrode, $LiPF_6$ in EC: DMC (1:2 vol%) as electrolyte and Celgard 2300 as separator within an argon filled glove box (M'BRAUN, Germany) where the moisture and oxygen levels were both kept below 1.0 ppm. Gavanostatic charge-discharge measurements were carried out using an automatic battery tester (Model: BT2000, Arbin, USA) in the potential window of 0.01- 3.0 V with a constant current density of 0.2 $mAcm^{-2}$ for both discharge and charge. Cyclic voltammetry experiments were carried out in the potential window of 0.01-3.0 V at a scan rate of 0.1 $mVs^{-1}$ using a Galvanostat-Potentiostat (Autolab 302N, The Netherlands). Electrochemical impedance spectroscopy (EIS) measurements were also carried out using the same Galvanostat-Potentiostat in the frequency range of 10 mHz-1.0 MHz at open circuit potential with an AC amplitude of 10 mV.

## Results and discussion

The desired porous $Mn_2O_3$ was obtained by calcination (at 500°C for 6 h) of $MnCO_3$ intermediates with varying shapes, synthesized by hydrothermal treatment of aqueous precursor solution containing ammonium carbonate, $MnCl_2$ and CA/ TA/ OA/ EDTA as chelating agents. The chelating agent controls the morphology of $MnCO_3$ intermediate.[19] The formation of $MnCO_3$ as intermediate and $Mn_2O_3$ on calcination was confirmed by XRD. All the as-synthesized



 

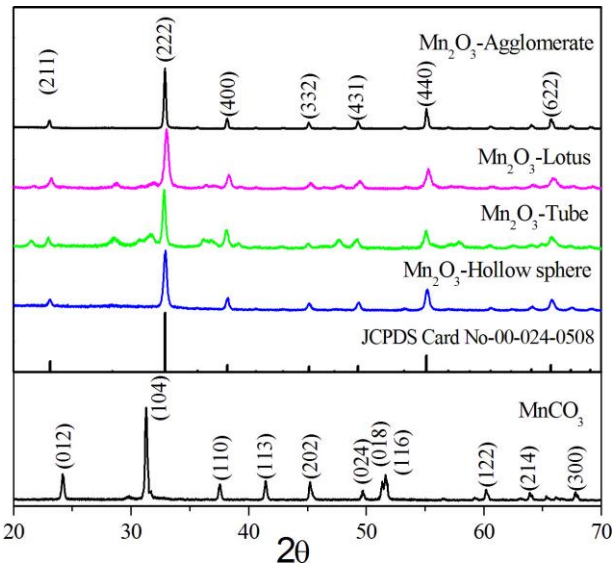


**Fig. 1** XRD pattern of the synthesized bare carbonate and calcined $Mn_2O_3$ with varying shapes.

intermediates synthesized in presence of varying chelating agent showed identical well resolved diffraction peaks and the peaks can be indexed to the rhombohedra $MnCO_3$ (JCPDS Card 83-1763) (Fig. 1) and absence of any additional peak confirmed the formation of phase pure carbonate intermediates. After calcination of carbonate intermediate all the samples resulted identical well resolved diffraction peaks except the calcined product of carbonate intermediate synthesized in presence of TA and can be indexed to orthorhombic $Mn_2O_3$ (JCPDS Card 24-0508) (Fig. 1). In the XRD pattern of calcined sample synthesized in presence of TA some additional peaks was observed which are nothing but the peaks of α-$Mn_2O_3$ (JCPDS Card 73-1826). In all the samples absence of any peak for carbonate or other additional peak indicate the total

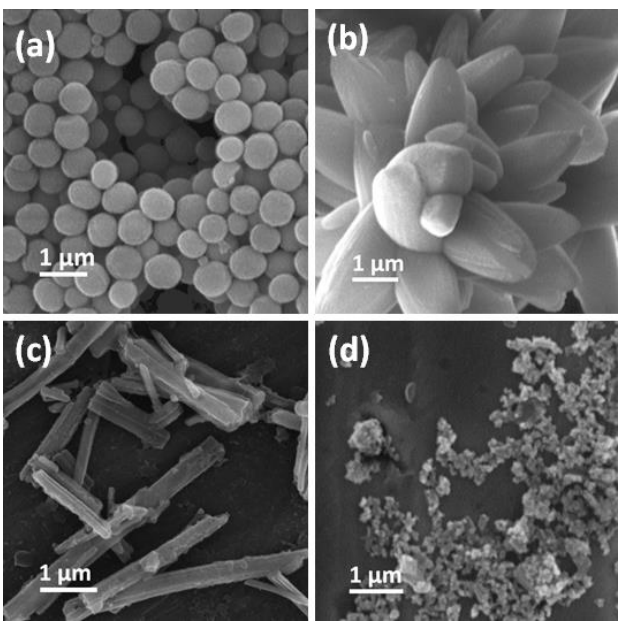


**Fig. 2** SEM images of bare $MnCO_3$ synthesized in the presence of (a) oxalic acid, (b) citric acid, (c) tartaric acid and (d) EDTA.

decomposition of carbonate phase and formation of phase pure $Mn_2O_3$. The average crystallite sizes of the synthesized $Mn_2O_3$ were found in the range of 25-35 nm, calculated from Debye Scherer's equation using X-ray line broadening of all individual diffractions and presented in Table 1. In the TG curve of as-synthesized $MnCO_3$ intermediate no weight loss was observed after 450 °C and confirm the total decomposition of $MnCO_3$ (Fig.S1, see ESI†).

**Table 1** Characteristic Morphology of the synthesized $Mn_2O_3$ with varying shapes.

| Morphology | $S_{BET}$ ( $m^2$ $g^{-1}$) | Pore Vol. ($cm^3/g$) | Pore Size (nm) | Cryst. size (nm) |
|---|---|---|---|---|
| Hollow Sphere | 25.9 | 0.461343 | 25.0101 | 24.9 |
| Tube | 28.8 | 0.296197 | 29.3707 | 32.1 |
| Lotus | 48.1 | 0.232655 | 14.6599 | 28.4 |
| Agglomerate | 19.7 | 0.147166 | 28.2542 | 35.3 |

$S_{BET}$=BET surface area, Cryst. Size= Crystalite size calculated from XRD line broadening

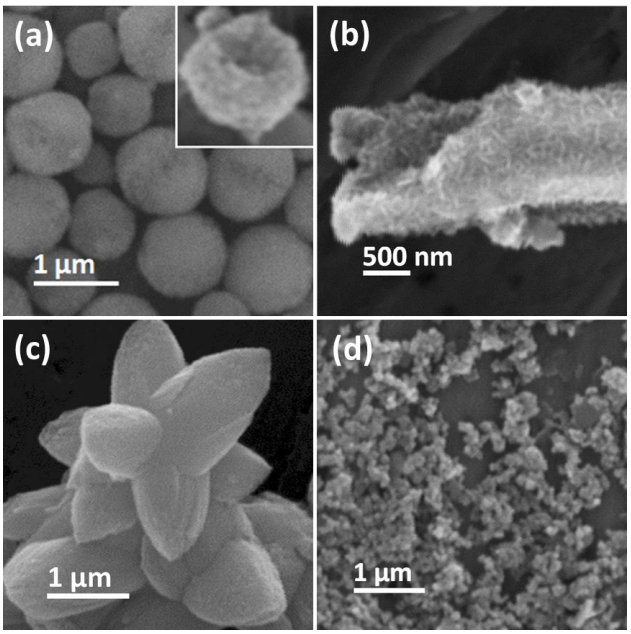


**Fig. 3** SEM images of $Mn_2O_3$ with varying shapes (a) hollow sphere and corresponding partially broken spheres (inset), (b) tube, (c) lotus shaped and (d) aggregated particles, obtained after calcination at 500 °C for 6h of the corresponding $MnCO_3$.

Fig. 2 represents the SEM images of as-synthesized $MnCO_3$ and found that the lotus, rod, spherical shaped (hollow) $MnCO_3$ intermediate were formed in presence of CA, TA, OA, respectively, in the precursor solution. Aggregated $MnCO_3$ particles were formed in presence of EDTA. From the SEM images it is evident that presence chelating ligand in the reaction mixture has a definite effect on morphology. All the bare carbonate intermediate resulted almost identical morphology on calcination at 500°C/6h (Fig. 3). But the microstructure became porous due to the decomposition of carbonate intermediate and evolution of $CO_2$ and $H_2O$. From the SEM images of calcined $Mn_2O_3$ with varying shapes, it is evident that the lotus shaped microstructures are nothing but a 3D assembly of the individual petals with ~ 4-6 µm length and 1-2 µm width in middle,

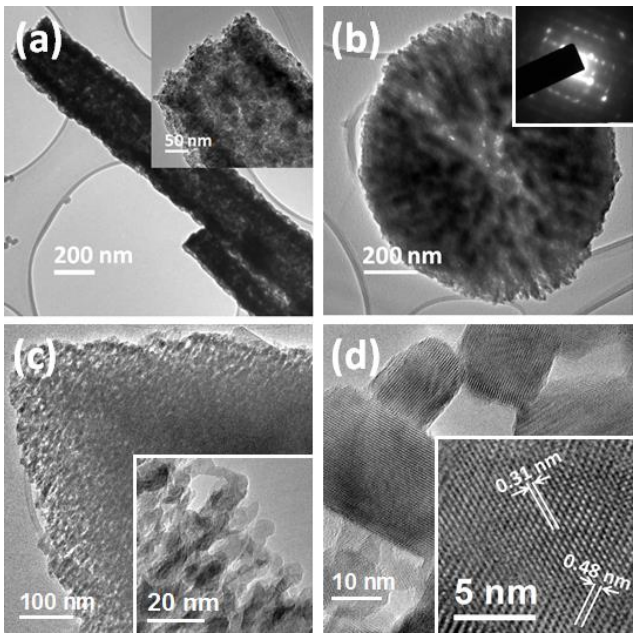


**Fig. 4** TEM images of calcined $Mn_2O_3$ with varying shapes (a) tubes, (b) hollow sphere, (c) petal of lotus shape and (d) aggregated particles.

rods are nothing but the tubes with ~ 4-12 µm length and 0.5-1.5 µm width and average radius of spheres are in the range of 0.5-2 µm. The SEM image of partially broken spheres (inset Fig. 3a) clearly depicts the hollow interior and demonstrates the hollow nature of the synthesized spheres.

TEM imaged of all the samples supports the morphological evaluation results obtained from SEM (Fig. 4). The TEM images of 1D rod further confirm that the rods are nothing but the tubes and spheres contains inner hollow spaces. TEM images of all the morphologies also confirmed the formation of porous structures with a broad pore size distribution. In the HRTEM images confirms that the microstructures were constructed of distinct nanoparticles in the size range of 20-40 nm and supports the crystallite size results obtained from XRD line broadening. The distinct lattice fringes with an inter-planer distance of 0.31 and 0.48 nm, assigned to (122) and (200) planes of orthorhombic $Mn_2O_3$.

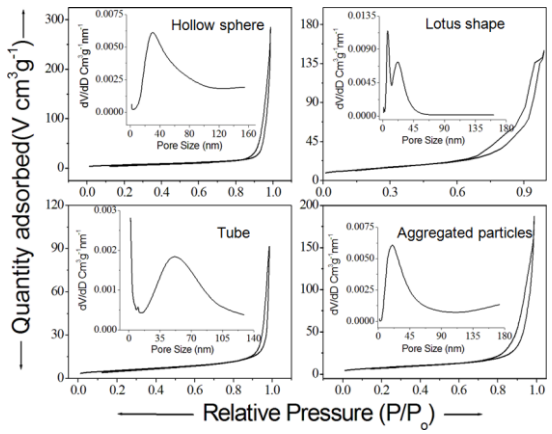


**Fig. 5** Nitrogen sorption isotherm and corresponding poresize distribution of synthesized $Mn_2O_3$ with varying shapes.

HR-TEM images confirmed that the materials are highly crystalline in nature and supports the XRD results (Fig. 4d). The electron diffraction pattern of all the samples indicates the synthesized $Mn_2O_3$ microstructures are polycrystalline in nature (inset Fig. 4b).

The Liquid-nitrogen cryosorption studies were performed to understand the textural properties and inner architectures of the synthesized $Mn_2O_3$ shapes. The $N_2$ sorption isotherm and corresponding BJH pore size distribution plots of all the $Mn_2O_3$ shapes were presented in Fig. 5. Estimation of surface area was performed from adsorption data in a relative pressure range from 0.05 to 1.0. All the isotherms are convex in nature up to p/p°~1 and can be assigning to Type III. All the synthesized $Mn_2O_3$ shapes, except lotus shape, showed distinct hysteresis loop within the p/p° region of >0.8 to 1 which is similar to the H3 type and revealed the presence of inter particle pores. Whereas, presence hysteresis loop at and before p/p° region of 0.8 to 1 in lotus shape revealed the mixed H1 and H3 type indicates the presence of some interconnected slit type pores with inter-particle pores. Thus the isotherm and corresponding hysteresis loop evidenced that the synthesized shapes are nothing but the 3D assembly of nanoparticles and only lotus shaped materials contained some structural pores with inter-particle pores. The pore size distribution, calculated from the adsorption part of the nitrogen sorption isotherm, of all the shapes, except lotus shape, reveals the presence of a broad pore size distribution in the range of 20-110 nm. Lotus shaped material contained two pore size distribution, a narrow pore distribution centered at ~8 nm and a broad size distribution centered at ~40 nm which are ascribed as structural pores and inter-particle pores, respectively. The BET surface area of the synthesized hollow sphere, tube, lotus shaped and aggregated particle were 26, 29, 48 and 19 $m^2g^{-1}$ with a pore volume of 0.46, 0.29, 0.23, 0.15 $cm^3g^{-1}$, respectively. Comparing BET surface area with pore volume of all the synthesized $Mn_2O_3$ shapes, it reveals the surface area of lotus shaped $Mn_2O_3$ is higher than that of tubular and hollow micro spherical $Mn_2O_3$ but the pore volume of earlier one is less than that of later two. This contradictory result can be explained by the presence of some blind pores, which was only contributes to surface area but not to the active pore volume, in the lotus shaped $Mn_2O_3$.

The adapted synthetic strategy is based on the synthesis of $Mn_2O_3$ through the calcination of $MnCO_3$ intermediate with varying shapes. A chelating mediated solution based synthetic route was used for the synthesis of $MnCO_3$ shapes using TA, CA, OA as chelating agent and aqueous solution of $MnCl_2$ and $(NH_4)_3CO_3$ as precursor solution. It was observed that the strength and geometry of the chelating agent are the prime controlling factor for the synthesis of the variation of shapes of $MnCO_3$. A detailed formation mechanism for chelate mediated growth of $MnCO_3$ shapes has already discussed in our previously report. [19] The mechanism is based on the formation of chelating agent capped $MnCO_3$ nuclei with varying orientation according to their geometry and strength in initial stage of synthesis. Then, the growth process followed the orientated attachment mechanism. For the geometrical variation of ligand, i.e., 3D and 2D arrangement of functional group of CA and



 

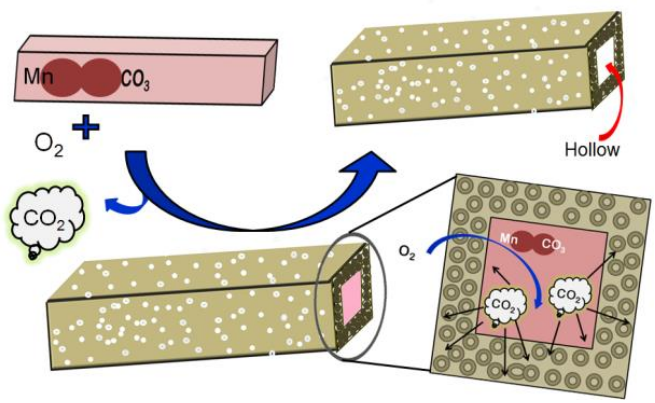


**Fig. 6** Schematic representation of probable formation mechanism of porous and tubular (hollow) $Mn_2O_3$ structure from corresponding rod shaped $MnCO_3$.

TA, respectively, CA resulted the 3D lotus shape and TA resulted 1D rods. However due to low chelating ability of OA, it gave solid sphere. Then on calcination the solid structures produced porous hollow structure. The porous structure was formed due to the decomposition of carbonate and during evolution to $CO_2$ the pores were generated in the microstructures. Whereas hollow structure were formed through a nonequilibrium interdiffusion process,[22] known as Kirkendall effect. During calcination the $MnCO_3$ oxidized and converted to $Mn_2O_3$ in presence of $O_2$ of air. In the thicker structure, like sphere or road, the outer surface of the structures were oxidised first and resulted a core-shell like structure where $Mn_2O_3$ is in shell and $MnCO_3$ in core. The interface of shell contains lots of vacancies. The $MnCO_3$ were diffuse to outwards through the vacancies. However, the rate of diffusion of $MnCO_3$ is higher than that of atmospheric oxygen during the oxidation reactions which creates the voids in interior core and eventually hollow cavity was generated. It was observed that calcination temperature and rate of increment of temperature has distinct effect on cavity. At higher heating rate, the hollow structure was destroyed, due to rapid decomposition of $MnCO_3$ and liberation of $CO_2$. In low heating rate a good hollow structure was formed for low diffusion rate. Similar, observations were also reported earliear for transition metal oxide.[23]

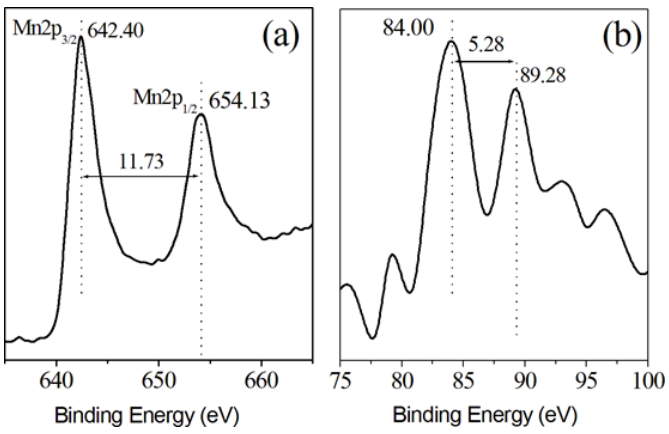


**Fig. 7** High resolution Mn2p and Mn3s XPS spectra of the synthesized $Mn_2O_3$ hollow spheres.

Fig. 6 represents a probable formation mechanism of $Mn_2O_3$ hollow tube from $MnCO_3$ rod as typical representative. Here it is essential to mentioned that although the spherical and rod shaped $MnCO_3$ resulted hollow structure; the hollow morphology of flower was not identified, which is most probably due to is low thickness of individual petal. Due to the low thickness of petal the core-shell structure was not formed and decomposition as well as oxidation took place quickly.

For more confirmation of the oxidation state of synthesized Mn-oxide we did XPS analysis. Because XPS is the only tool for the confirmation of surface composition. In the high resolution XPS, the two Mn2p peak at 642.40 and 654.13 eV, with a spin energy gap of 11.73, can be assigned to $Mn2p_{3/2}$ and $Mn2p_{1/2}$, respectively (Fig. 7a). It is difficult to gate a solid conclusion about the oxidation state of manganese from Mn2p spectra, as all manganese oxidation state show same pattern. So, core Mn 3s XPS became crucial for the determination of oxidation state of Mn. The core Mn 3s XPS multiplet splitting peaks only give the idea about the valence state of the manganese because of the splitting width was different for different valance state.[24] This splitting arise due to exchange interaction of core 3s and unpaired 3d valence electron level leading to photoelectron ejection.[24] According to Chigane *et al.*, the multiplate splitting for $Mn^{3+}$ is 5.3 and with decreasing the oxidation state the splitting gap increases. In present synthesized $Mn_2O_3$ samples the Mn3s XPS spectrum resulted the splitting of ($\Delta E$) 5.28 eV (Fig. 7b). This value is higher than the value for $Mn^{3+}$ oxidation state which indicates that in our materials only contain the pure $Mn^{3+}$ oxidation state. Thus, we can conclude that the synthesized materials are pure $Mn_2O_3$.

**Electrochemical Application.**

Electrochemical properties of the synthesized $Mn_2O_3$ samples were first investigated by cyclic voltammetry to understand the redox processes. Fig. 8a shows first three successive scans (for $Mn_2O_3$ sphere) in the voltage range 0.01-3.0 V at a scanning rate of 0.1 $mVs^{-1}$. During the first scan, a broad cathodic peak centered around 1.16 V indicates conversion of $Mn^{3+}$ to $Mn^{2+}$.[9, 15] A second sharp cathodic peak observed at ~0.18 V originates from the conversion of $Mn^{2+}$ to $Mn^0$ along with formation of $Li_2O$ and also, from the irreversible reactions of organic carbonates in the electrolyte with Li at this low potential forming a SEI layer.[25-26] The minor peaks observed at ~0.94 and 0.71 V may be due to irreversible partial decomposition of the organic solvents. During the first anodic scan, only one relatively broad peak is observed at ~1.36 V indication oxidation of $Mn^0$ to $Mn^{2+}$ and partial decomposition of $Li_2O$ to Li.[9, 15] Absence of any peak at higher voltages (up to 3.0 V) indicates no further oxidation of Mn. Consequently, in the subsequent cycles no peak is observed at 1.16 V during the cathodic scan. From the second cycle onwards, the CV consists of a single cathodic peak and the corresponding anodic peak due to the reversible conversion reaction, $Mn^{2+} \leftrightarrow Mn^0$. However, a shifting of peak position is observed for the cathodic process with reduction of peak intensity which indicates that the irreversible reactions occurring during the first scan are absent. Thus, the results in CV are in perfect agreement with the reported electrochemical reaction in $Mn_2O_3$ based on conversion mechanism:[9, 21]

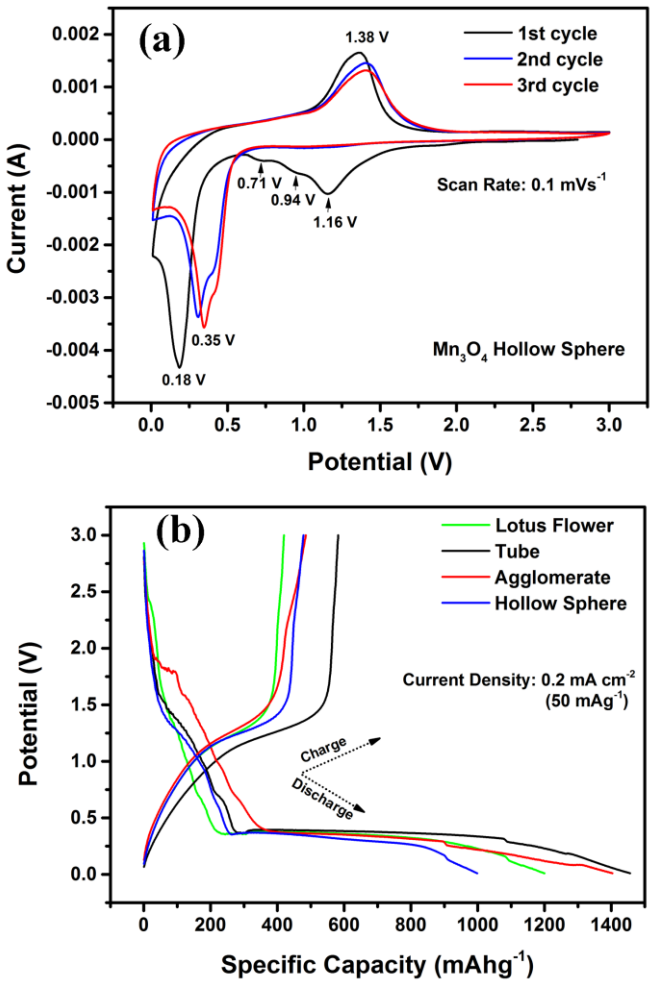


**Fig. 8** (a) Three successive cyclic voltammetry scans for an as-assembled $Mn_2O_3$ hollow sphere //Li cell (b) initial discharge-charge profiles of $Mn_2O_3$//Li cells

$$2Li^{+}+3Mn_2O_3+2e^{-}\rightarrow 2Mn_3O_4+Li_2O \quad (1)$$

$$2Li^{+}+Mn_3O_4+2e^{-}\rightarrow 3MnO+Li_2O \quad (2)$$

$$MnO+2Li^{+}+2e^{-}\leftrightarrow Li_2O+Mn \quad (3)$$

$$Mn + x\ Li_2O \leftrightarrow 2x\ Li^{+}+ MnO_x + 2x\ e^{-}\ (1.0 < x < 1:5) \quad (4)$$

Fig. 8b shows the galvanostatic discharge-charge profiles for the synthesized $Mn_2O_3$ with different shapes in the potential range 0.01 – 3.0 V at a current density of 0.2 $mAcm^{-2}$. Except for the agglomerate, the observed plateaus in the discharge and charge profiles of the $Mn_2O_3$ samples (lotus flower, tube and hollow sphere) corroborate the observation of CV for the hollow sphere sample (Fig. 8). For the agglomerate sample, the first reduction plateau ($Mn^{3+} \rightarrow Mn^{2+}$) is upshifted to ~1.75 V. Also, there is a small kink at ~2.3 V during the charge process indicating oxidation of $Mn^{2+}$ to $Mn^{3+}$ which is not observed for other samples indicating that the morphologies of these manganese oxide materials have a significant effect on their electrochemical behaviour. Observation of the $Mn^{2+}$ to $Mn^{3+}$ oxidation peak has also been reported for porous $Mn_2O_3$ microspheres [15] and nanoplates.[9] The charge capacities for lotus flower, tube, agglomerate and hollow sphere $Mn_2O_3$ are found to be 420, 582, 485 and 478 $mAhg^{-1}$ respectively with corresponding first cycle Columbic efficiencies of 35%, 40%, 34% and 48% . Low Columbic efficiencies are commonly observed for metal oxides with conversion reactions and can be attributed to electrochemical participation of the electrolyte and consumption of Li in the SEI layer.[27] Although the agglomerate shows the highest initial charge capacity, it has the lowest Columbic efficiency indicating more side reactions and probable interfacial Li storage such as, $Li/Li_2O$ interface.[18]

Fig. 9a shows the cycling performance of the synthesized $Mn_2O_3$ with different shapes in the potential range 0.01–3.0 V at a current density of 0.2 $mAcm^{-2}$. A sharp decrease in capacity with increasing cycle number is observed up to ~30 cycles for all samples irrespective of the shape and thereafter a steady value is obtained. At the 50$^{th}$ cycle, only 33%, 28%, 23% and 38% of capacity is retained with respect to the initial capacity for lotus flower, tube, agglomerate and hollow sphere $Mn_2O_3$ respectively (also see Fig.S2, ESI†). Such cycling performance is commonly observed for metal

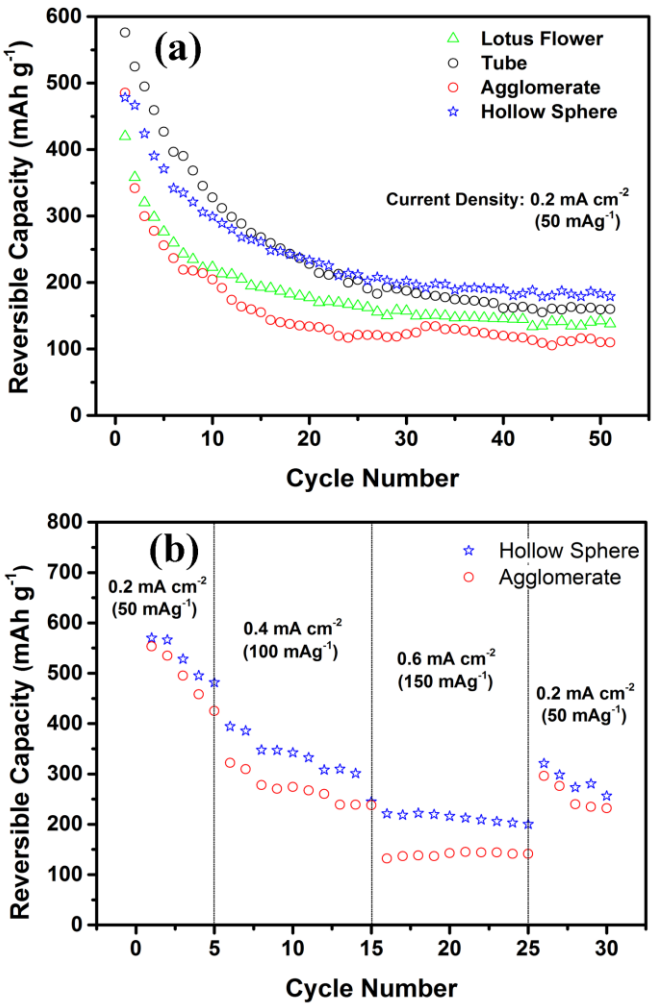


**Fig. 9.** Electrochemical performance of the synthesized $Mn_2O_3$ with different shapes (a) cycling behaviour (b) rate performance

oxides where the electrochemical reactions proceed through a conversion mechanism, owing to the large specific volume change during lithiation and delithiation. In the present case, different shapes and sizes lead to different morphologies and different pore volume with different pore size, which was may cause for different specific capacity.[28] In the agglomerates, low surface area and low pore volume results in a poor cycling performance. The lotus flower sample, though has the highest surface area, contains bimodal distribution with blind pores inaccessible to the electrolyte. On the other hand, the highest pore volume in the hollow sphere leads to an increased effective electrode/electrolyte interface area due to presence of both kinds of pores, meso pores increase the ion transportance and macropores behaves as a reservoir for bulk electrolyte into the hollow structure,[28] resulting in a superior performance compared to others. Additionally, in the hollow spheres, the volume changes and subsequent pulverization are supressed to a large extent by their ability to accommodate transformation strains within the porous structure during cycling. That the observed capacities are significantly lower than the theoretical capacity of $Mn_2O_3$ (1018 $mAhg^{-1}$) may be due to higher loading of the active material (75 wt%) compared to those reported in literature.[9, 15] $Mn_2O_3$ being a poor electronic conductor, such high loading may result in limited inter-grain charge transfer. Impedance spectroscopy shows that the as-assembled cells have low solution resistance $R_s$ in the range of 4.1-7.3 Ω and charge transfer resistance ($R_{ct}$) in the range of 242-450 Ω (Fig. S3 and Table S1, ESI†). However, it has been found that with cycling $R_{ct}$ becomes minimum for the hollow spheres indicating higher rate of inter-grain charge transfer (Fig. S4, ESI†). However, it appears that the thickness of the SEI layer significantly increases with cycling for all samples explaining the observed fading in capacity. The superior performance of hollow sphere $Mn_3O_4$ is also manifested in the rate performance study, shown in Fig.9b. At each current density, ranging from 0.2 $mAcm^{-2}$ to 0.6 $mAcm^{-2}$, the rate capability as well as capacity restoration of hollow sphere is superior to that of agglomerates though the initial capacity is the same for both samples.

## Conclusions.

In conclusion, we have developed a facile strategy for synthesis of porous 3D assembled $Mn_2O_3$ architectures with varying shapes; hollow sphere, lotus shaped and tubular, as well as aggregated nanoparticles; through calcination of corresponding $MnCO_3$ intermediate with identical morphology. Porous hollow structures were formed due to the evolution of $CO_2$ during decomposition of carbonate intermediate and hollow structure were formed through nonequilibrium interdiffusion process, i.e., Kirkendall effect. Electrochemical results demonstrate that Li- ion storage capacity and cycling behavior of synthesized $Mn_2O_3$ is strongly influenced by the shape. Compared to the agglomerates, all porous samples with 3D architecture with different shapes show a better columbic efficiency and capacity retention upon cycling. The lithiation and delithiation process are mainly controlled by the total surface area, type of pores and their size of 3D architectures. Hollow spheres showed highest specific capacity of 478 $mAhg^{-1}$ with 38% retention after 50 cycles.

## Acknowledgements

The authors are thankful to Department of Science and Technology, India (DST, SR/S1/IC-33/2011) for financial support for this work. Authors also acknowledge "Analytical Discipline and Centralized Instrumental Facilities" of CSIR-CSMCRI for providing instrumentation facilities. PP and AKG acknowledge CSIR, India, for a research fellowship and also thankful to AcSIR for enrolment in Ph.D. SM and ABP thanks to Director, CSIR-CGCRI for his kind permission for the collaborative research.

## Notes and references

[a] Discipline of Inorganic Materials and Catalysis and Academy of Scientific and Innovative Research, CSIR-Central Salt and Marine Chemicals Research Institute, G.B. Marg, Bhavnagar-364021, India, e-mail: abpanda@csmcri.org.

[b] Fuel Cell & Battery Division, CSIR-Central Glass and Ceramic Research Institute, Kolkata-700032, India.

**Electronic Supplementary Information** (ESI) available: [TG, Discharge-charge profiles and Impedance spectra]. See DOI: 10.1039/b000000x/

1 (a) E. Roduner, Nanoscopic Materials: Size-Dependent Phenomena, RSC Publications, Cambridge, UK, 2006; (b) C. Burda, X. Chen, R. Narayanan and M. A. El-Sayed, *Chem. Rev.*, 2005, **105**, 1025-1102.

2 J. N. Tiwari, R. N. Tiwari, and K. S. Kim, *Prog. Mater. Sci.*, 2012, **57**, 724–803.

3 (a) X. Wang, J. Zhuang, Q. Peng and Y. Li, *Nature*, 2005, **437**, 121-124; (b) X. Huang, C. Tan, Z. Yin and H. Zhang, *Adv. Mater.*, 2014, **26**, 2185–2204; (c) Y.-W. Jun, J.-S. Choi and J. Cheon, *Angew. Chem. Int. Ed*., 2006, **45**, 3414 – 3439; (d) M. R. Buck and R. E. Schaak, *Angew. Chem. Int. Ed*., 2013, **52**, 6154 – 6178; (e) S. K. Pahari, A. Sinhamahapatra, N. Sutradhar, H. C. Bajaj and A. B. Panda, *Chem. Commun*., 2012, **48**, 850–852; (f) P. Pal, S. K. Pahari, A. Sinhamahapatra, M. Jayachandran, G. V. M. Kiruthika, H. C. Bajaj and A. B. Panda, *RSC Adv.*, 2013, **3**, 10837–10847.

4 (a) C. T. Cherian, M. V. Reddy, S. C. Haur and B. V. R. Chowdari, *ACS Appl. Mater. Interfaces*, 2013, **5**, 918−923; (b) B. Liu, J. Zhang, X. Wang, G. Chen, D. Chen, C. Zhou and G. Shen, *Nano Lett*., 2012, **12**, 3005−3011; (c) A. Sinhamahapatra, A. K. Giri, P. Pal, S. K. Pahari, H. C. Bajaj and A. B. Panda, J. Mater. Chem., 2012, **22**, 17227-17235; (d) M. Law, E. Greene, J. C. Johnson, R. Saykally and P. Yang, Nature Mater., 2005, 4, 455-459.

5 (a) V. Polshettiwar, B. Baruwati and R. S. Varma, *ACS Nano.*, 2009, 3, 728-736; (b) K. Miszta, J. D Graaf, G. Bertoni, D. Dorfs, R. Brescia, S. Marras, L. Ceseracciu, R. Cingolani, R. Roij, M. Dijkstra and L. Manna, *Nat. Mater* , 2011, **10**, 872–876; (c) G. Divitini, O. Stenzel , A. Ghadirzadeh , S. Guarnera , V. Russo ,C. S. Casari , A. L. Bassi , A. Petrozza , F. D. Fonzo ,V. Schmidt , C. Ducati, *Adv. Funct. Mater*., 2014, **24**, 3043–3050; (d) H. Zhu, M. L. Du, M. Zhang, M. L. Zou, T. T. Yang, Y. Q. Fu and J. M. Yao,. *J Mater. Chem. A*, 2014, **2**, 7680-7685; (e) C. Yuan, H. B. Wu, Y. Xie and X. W. Lou, *Angew. Chem. Int. Ed.*, 2014, **53**, 1488 – 1504.

6 (a) G. Zhang, B. Y. Xia, C. Xiao, L. Yu, X. Wang, Y. Xie and X. W. Lou, *Angew. Chem. Int. Ed.*, 2013, **52**, 8643 –8647; (b) H. Zhang, H. Wang, Y. Xu, S. Zhuo, Y. Yu and B. Zhang, *Angew. Chem. Int. Ed.*, 2012, **51**, 1459 –1463; (c) G. Zhang, X. Shen and Y. Yang, *J. Phys. Chem. C*, 2011, **115**, 7145-7152; (d) J. Liu, T. Luo, S. T. Mouli, F. Meng, B. Sun, M. Li and J. Liu, *Chem. Commun.*, 2010, **46**, 472-474; (e) J. Liu, H. Xia, L. Lu and D. Xue, *J. Mater. Chem.*, 2010, **20**, 1506-1510; (f) N. Sutradhar, A. Sinhamahapatra, S. K. Pahari, M.

Jayachandran, B. Subramanian, H. C. Bajaj and A. B. Panda, *J. Phys. Chem. C*, 2011, **115**, 7628-7637; (g) N. Sutradhar, A. Sinhamahapatra, S. K. Pahari, P. Pal, H. C. Bajaj, I. Mukhopadhyay, and A. B. Panda, *J. Phys. Chem. C*, 2011, **115**, 12308-12316; (h) A. K. Giri, A. Sinhamahapatra, S. Prakash, J. Chaudhari, V. K. Shahi and A. B. Panda, *J. Mater. Chem. A*, 2013, **1**, 814-822;

7 (a) S. Ching, D. A. Kriz, K. M. Luthy, E. C. Njagi and S. L. Suib, *Chem. Commun.*, 2011, **47**, 8286-8288; (b) C. Yuan, L Hou, L Yang, D. Li, L. Shen, F. Zhang and X. Zhang, *J. Mater. Chem.*, 2011, **21**, 16035-16041; (c) L. Espinal, W. Wong-Ng, J. A. Kaduk, A. J. Allen, C. R. Snyder, C. Chiu, D. W. Siderius, L. Li, E. Cockayne, A. E. Espinal and S. L. Suib, *J. Am. Chem. Soc*., 2012, **134**, 7944−7951; (d) A. K. Sinha, M. Basu, M. Pradhan, S. Sarkar, Y. Negishi and T. Pal, *J. Phys. Chem. C* 2010, **114**, 21173.

8 (a) J. Cao , Q. Mao and Y. Qian, *J. Solid State Chem.*, 2012, **191**, 10–14; (b) Y. Ren, Z. Ma, L. Qian, S. Dai, H. He and P. G. Bruce, *Catal Lett*., 2009, **131**, 146–154; (c) Y. Wang, Y. Wang, D. Jia, Z. Peng, Y. Xia and G. Zheng, *Nano Lett*., 2014, **14**, 1080−1084.

9 Y. Zhang, Y. Yan, X. Wang, G. Li, D. Deng, L. Jiang, C. Shu and C. Wang, *Chem. Eur. J.*, 2014, **20**, 1–6.

10 Y. Qiao, Y. Yu, Y. Jin, Y.-B. Guan and C.-H. Chen, *Electrochimica Acta*, 2014, **132**, 323–331.

11 Y. Dai, H. Jiang, Y. Hu and C. Li, *RSC Adv.*, 2013, **3**, 19778-19781.

12 Y. Cai, S. Liu, X. Yin, Q. Hao, M. Zhang and T. Wang, *Physica E*, 2010, **43**, 70–75.

13 M.-W. Xu, Y.-B. Niu, S.-J. Bao and C. M. Li, *J. Mater. Chem. A*, 2014, **2**, 3749-3755.

14 (a) J J. Cao, Y. Zhu, K. Bao, L. Shi, S. Liu and Y. Qian, *J. Phys. Chem. C*, 2009, **113**, 17755–17760; (b) L. Chang, L. Mai, X. Xu, Q. An, Y. Zhao, D. Wang and Xi Feng, *RSC Adv.*, 2013, **3**, 1947-1952.

15 Y. Deng, Z. Li, Z. Shi, H. Xu, F. Peng and G. Chen, *RSC Adv*., 2012, **2**, 4645–4647.

16 X. Zhang, Y. Qian, Y. Zhu and K. Tang, *Nanoscale*, 2014, **6**, 1725-1731.

17 (a) W.-N. Li, L. Zhang, S. Sithambaram, J. Yuan, X.-F. Shen, M. Aindow and S. L. Suib. *J. Phys. Chem. C*, 2007, **111**, 14694-14697; (b) H. Cao, X. Wu, G. Wang, J. Yin, G. Yin, F. Zhang and J. Liu. *J. Phys. Chem. C*, 2012, **116**, 21109−21115.

18 Y. Qiu, G.-L. Xu, K. Yan, H. Sun, J. Xiao, S. Yang, S.-G. Sun, L. Jind and H. Deng, *J. Mater. Chem.*, 2011, **21**, 6346-6353.

19 P. Pal, S. K. Pahari, A. K. Giri, S. Pal, H. C. Bajaj and A. B. Panda, *J. Chem. Mater. A*, 2013, **1**, 10251-10258.

20 H. W Shim, A. H. Lim, K. M. Min and D. W. Kim, *CrystEngComm* 2011, **13**, 6747−6752.

21 Q. Li, L. Yin, Z. Li, X. Wang, Y. Qi, and J. Ma, *ACS Appl. Mater. Interfaces* 2013, **5**, 10975−10984.

22 W. Wang, M. Dahl and Y. Yin, *Chem. Mater.*, 2013, **25**, 1179−1189.

23 J. Liu and D. Xue, *Adv. Mater.*, 2008, **20**, 2622–2627.

24 M. Chigane and M. Ishikawa, *J. Electrochem. Soc.*, 2000, **147**, 2246-2251.

25 L. F. Xiao, Y. Y. Yang, J. Yin, Q. Li and L. Z. Zhang, *J. Power Sources*, 2009, **194**, 1089-1093.

26 Y. Ren, A. R. Armsrong, F. Jiao and P. G. Bruce, *J. Am. Chem. Soc.*, 2010, **132**, 996-1004.

27 X. H. Wang, X. W. Li, X. L. Sun, F. Li, Q. M. Liu, Q. Wang and D. Y. He, *J. Mater.Chem.*, 2011, **21**, 3571.

28 D.-W. Wang, F. Li, M. Liu, G. Q. Lu and H.-M. Cheng, *Angew. Chem. Int. Ed.* 2008, **47**, 373 – 376.



 